Optics Letters

Self-mode-locking in a high-power hybrid silicon nitride integrated laser

Yvan Klaver,[1,*] Jörn P. Epping,[2] Chris G. H. Roeloffzen,[3] and David A. I. Marpaung[1]

[1]Laser Physics and Nonlinear Optics, Mesa+ Institute for Nanotechnology, Department for Science and Technology, Applied Nanophotonics, University of Twente, 7522 NB Enschede, The Netherlands
[2]QuiX BV, 7521 AN Enschede, The Netherlands
[3]LioniX International BV, 7521 AN Enschede, The Netherlands
*Corresponding author: y.klaver@utwente.nl

Received 18 August 2021; revised 17 November 2021; accepted 17 November 2021; posted 18 November 2021; published 24 December 2021

Integrated mode-locked lasers are useful tools in microwave photonic applications as a local oscillator. In particular, hybrid integrated lasers could easily be integrated with passive processing circuits. In this Letter, we report on the self-mode-locking of a hybrid integrated laser comprising two indium phosphide gain sections and a silicon nitride feedback circuit that filters light using two ring resonators. The hybrid laser is shown to mode-lock and to have a mostly frequency-modulated field in the cavity using a stepped-heterodyne optical complex spectrum analysis. A mostly frequency modulated field output is good for high powers per line due to a more continuous emission, compared with mode-locked lasers using a saturable absorber; additionally, the filter limits the bandwidth of the comb, condensing the power to the fewer comb lines.

https://doi.org/10.1364/OL.440898

Optical frequency combs (OFCs) have found importance in a wide range of applications including precision spectroscopy [1], accurate time and frequency measurements [2], accurate optical ranging in LIDAR [3], and dense data transmission [4]. Recently, more effort has been spent in integrating OFCs in photonic circuits, for example, by including nonlinear resonators [5–7] and by integrated mode-locked lasers (MLLs) [8,9]. In particular, integrated MLLs can give unique comb characteristics for lower frequency ranges, which is particularly important for applications such as microwave photonics (MWP) [10]. The coherence between the comb lines will affect the purity of the radio-frequency (RF) signals generated from such a MLL.

Integration of lasers with larger-scale processing circuits can be achieved through hybrid integration. For example, combining semiconductor optical amplifiers (SOAs) in III-V with low loss circuits [11] can lead to a single-frequency laser with extremely low fundamental noise [12,13]. Recently, there has been interests in the demonstrations of mode-locking using hybrid integration approach [14–19], with the promise of integrable low-noise MLLs. However, despite recent progress, a few key ingredients leading integrable MLLs are missing. Most notably, the comb behavior in such hybrid lasers is not well studied and the clear indication through investigation of the mode-locking behaviors in such lasers is, to the best of the authors; knowledge, currently missing. The understanding of this comb and mode-locking behaviors will lead to markedly improved design with significant impact towards future implementation in MWP systems.

In this Letter, we show the mode-locked operation of a hybrid integrated laser comprising two gain sections, recently developed for high-power operation [20]. To ensure mode-locking and find the temporal behavior of the laser, we further study the MLL behavior through stepped-heterodyne optical complex spectrum analysis [21]. We found that the intracavity field of the laser during mode-locked operation is mostly frequency modulated, which is a property also observed with continuous-wave (CW) mode-locked diode lasers that lack filtering low-loss feedback circuit [22–24]. The result of this work paved the way to incorporate hybrid MLLs onto a low-loss silicon nitride platform for microwave photonic processing.

Our dual-gain laser has two indium phosphide (InP) gain sections connected to a silicon nitride (Si_3N_4) feedback circuit [25]. The feedback circuit performs a number of key functions including forming the laser cavity by connecting high reflective facets at each gain section and filtering the generated light via a ring resonator-based Vernier filter. The feedback circuit is controlled using thermo-optic tuning and the output, marked as P3 in Fig. 1, was primarily used for CW operation. The emission at this output can be controlled by the set of tunable couplers, TC1 and TC2, that regulates the fraction of power coupled out of the laser cavity and interferes the backward and forward propagating field coupled out from the cavity, respectively. To control detuning between the laser cavity resonance and Vernier filter peak, the laser is also equipped with on-chip phase shifters located directly after each gain section, as indicated by phase 1 and phase 2 in Fig. 1.

The laser predominantly showed two modes of operation, when operated under the condition where a single laser cavity mode is located in the passband of the Vernier filter, the laser shows single frequency behavior [20]. However, under the operation where the two cavity modes with lowest loss reach comparable attenuation by the ring resonators, we observed lasing at multiple frequencies. For such multiple-frequency

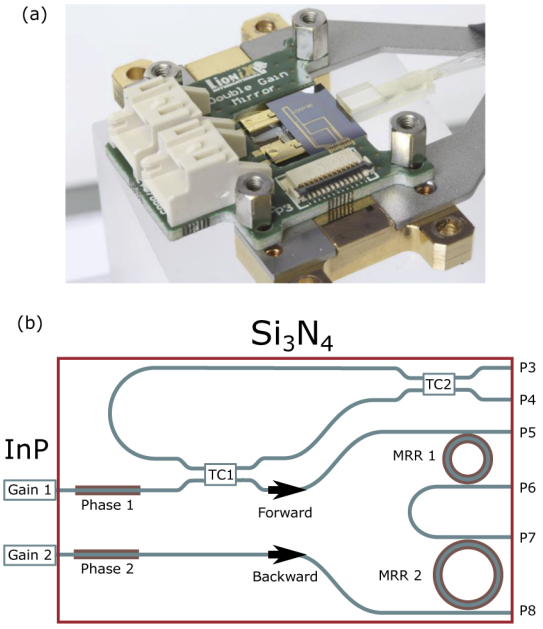

Fig. 1. (a) Photo of the assembled hybrid integrated laser [11]. (b) Schematic view of the hybrid laser comprising two InP gain sections and an Si_3N_4 feedback circuit that extends the cavity length optically via two ring resonators. The cavity mirrors are formed by the highly reflective (HR) coating on the back facet of each gain section. The light is coupled out of the cavity using a set of tunable couplers. P3 to P8 are test ports of the laser cavity over which the output field can be monitored.

lasing, we want to confirm that mode-locking appears. In any MLL the necessary condition to meet is that the output field E_{MLL} has both an envelope and instantaneous frequency that varies periodically, where the spacing between the lasing modes Ω determines the period of the envelope and instantaneous frequency.

In a MLL, the lasing modes can be described as phase-locked, as the phases of the different modes have a set relation ϕ_m after each period $2\pi/\Omega$. This can be summarized in the following expression [24]:

$$E_{\mathrm{MLL}}(t) = \exp\left(i\omega_s t + \phi_s(t)\right) \sum_{m=-N_L}^{N_U} \left(E_m \exp\left(i\left(m\Omega t + \phi_m\right)\right)\right), \quad \textbf{(1)}$$

where ω_s is the frequency of the center mode, $\phi_s(t)$ represents the optical phase noise, and E_m is the amplitude of each mode field. Although the spectral phase of each optical mode is dependent on time, the phase difference of the different modes should be independent of time given by $d\phi_k = \phi_{k+1} - \phi_k$. This phase difference could be retrieved using heterodyne detection of modes k and $k+1$. By retrieving this information for all pairs of neighboring modes, the complex spectrum of the laser output can be characterized and the time trace can be reconstructed. However, for the heterodyne detection of $d\phi_k$ for each pair of neighboring modes, these modes need to be isolated.

Stepped-heterodyne optical complex spectrum analysis, developed by Reid *et al.* [21], is the technique we implement to investigate experimentally the mode-locking behavior of our laser. The setup used is shown in Fig. 2, in this method a tunable CW light source is added as a local oscillator (LO) tuned in frequency between a pair of comb lines of the MLL, each measurement will give the phase difference $d\phi_k$ for the pair of comb lines the LO is placed between. Mixing the combined light source in a photo-diode will result in three tones of interest which are digitally filtered from a recorded oscilloscope trace using a band-pass filter, we used a raised cosine finite impulse response (FIR) filter with a bandwidth of 50 MHz. Two of the tones are a result of the LO mixing with the comb lines resulting in frequencies δ and Ω–δ, mixing the filtered tones in turn leads to a sum frequency signal representing the beating between the comb lines itself at a frequency Ω with the phase to measure $d\phi_k$. As a reference signal for the phase measurement we use the fundamental beat note Ω of the MLL, which if properly mode-locked should be of the same frequency and phase-locked to the beat note of the two comb lines.

We validate the mode-locking condition by showing the phase relation between two neighboring comb lines when the laser operates in two different states by tuning the heaters on the rings, tunable couplers, and phase section, one state with an optical spectrum of clearly visible lines and one where the laser

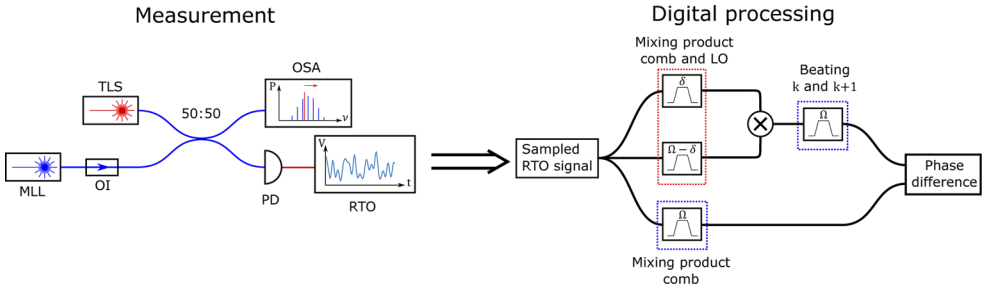

Fig. 2. Schematic of the setup both as a physical measurement and the digital processing of the acquired real-time oscilloscope (RTO) signal as described in [21]. In the measurement we combine a tunable laser source (TLS) with the mode-locked laser (MLL) which has an optical isolator (OI) placed at the output, in this case the hybrid laser, using a 2×2 50:50 directional coupler. The TLS is stepped in between each pair of comb lines which is monitored using an optical spectrum analyser (OSA) at one of the directional coupler outputs. On the other coupler output, the light is mixed in a photodiode (PD) and the resulting RF signal is sampled and saved by a RTO. After retrieving, the digital signal is then filtered for three frequency components, δ, Ω–δ and Ω, where δ and Ω–δ are the frequency difference between the LO and the comb lines the LO was placed in between. After filtering frequency components δ and Ω–δ are mixed which retrieves the beating signal of the comb lines the LO was placed in between. This signal is then compared with the fundamental beat signal of the comb in order to retrieve the phase difference $d\phi$.

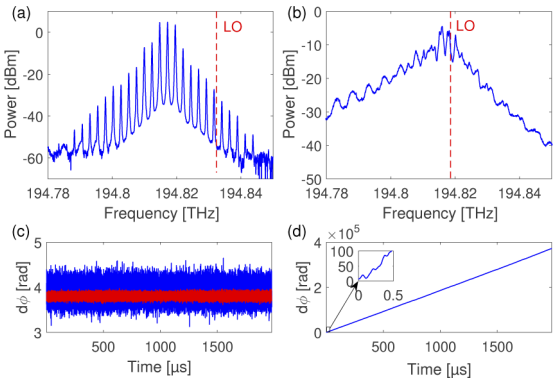

Fig. 3. Optical spectra found at the laser output (port P3) for two operation points (a) and (b) and the recorded phase difference when the local oscillator (LO) is placed at the frequencies as indicated with the dashed lines in (a) and (b). For the frequency comb shown in (a) the phase difference between the comb lines neighboring the LO is shown in (c); the wide trace gives an initial measurement and the narrow trace is a measurement performed 2 hours later with a higher sensitivity of the oscilloscope. For the low-coherence spectrum shown in (b), the phase difference is shown in (d) with an inset zoomed into the first 0.5 μs.

operates with a broad spectrum with barely visible lines, see Figs. 3(a) and 3(b), respectively. In Fig. 3(d) it is shown that the phase difference for the low-coherence comb does not observe a phase lock and has a predominantly linear relation signifying a frequency difference between the frequency of the largest beating power of the comb and the beating of the pair of comb lines investigated, in this case the slope accounts to a frequency difference of 29.8 MHz. For the comb with distinct lines in Fig. 3(a), we measured the phase difference between a pair of comb lines that are positioned next to the LO indicated in the figure, this phase difference shown in Fig. 3(c) shows stability over the maximum recording duration of the real-time oscilloscope (2 ms at 20 GSa/s). Moreover, the phase difference of the same pair is recorded 2 hours later with a higher resolution, i.e., 8 bit with a range of −25 to 25 mV instead of −175 to 175 mV and is shown as the narrow trace of Fig. 3(c) showing the value falls within the same range as the prior measurement for $d\phi$ represented as the wide trace. With the phase locking of the individual comb lines to the rest of the comb it is shown that the laser is operating in a mode-locked condition.

A reconstruction of the intracavity optical field is performed on a complete measurement of the complex optical spectrum shown in Fig. 4 using Eq. (1), and gives insight into the modulation present on the light. The complex spectrum is measured at test ports P5–P8 and corrected for the filtering induced by the ring resonators acting as add-drop resonators, to find the complex spectrum in the cavity just before the rings. For the laser operating point investigated with 150 mA on each gain section, the measured output spectra are shown as solid lines in Figs. 4(a) and 4(b). In this state, the power leaking from the filter and limited injection current limits the output power to 9.3 dBm in port 4 compared with the 19.3 dBm as demonstrated in [20]. After correcting for the filtering of the rings both with the frequency-dependent attenuation and phase delay, the power per spectral line and phase differences are shown as crosses and pluses, such that in Fig. 4(a) it shows the complex spectrum for the forward direction and in Fig. 4(b) for the backward direction with the directions as indicated in Fig. 1. The Vernier filter transmission corresponding to the correction applied on the spectra in Figs. 4(a) and 4(b) can be found in Fig. 4(c) shown as the solid line. In addition the Vernier filter adds an additional delay per round trip around the pass band, in Fig. 4(c) this band is shown as the reduction of the inverse group delay, where the inverse group delay is a first-order approximation of the free spectral range (FSR; see Supplement 1 for details). Close to the transmission peak of the Vernier filter the inverse group delay is close to the measured repetition rate of the optical signal $\Omega/2\pi = 2.48$ GHz. Finally, in Fig. 4(d) the intracavity power and instantaneous frequency difference from the carrier frequency over time can be found, which is reconstructed from the spectra measured at port 5. The instantaneous frequency difference from the carrier frequency in this case is defined as

$$df(t) = \frac{1}{2\pi}\left(\frac{d}{dt}\left(\arg\left(E_{\mathrm{MLL}}(t)\right)\right) - \omega_s\right). \tag{2}$$

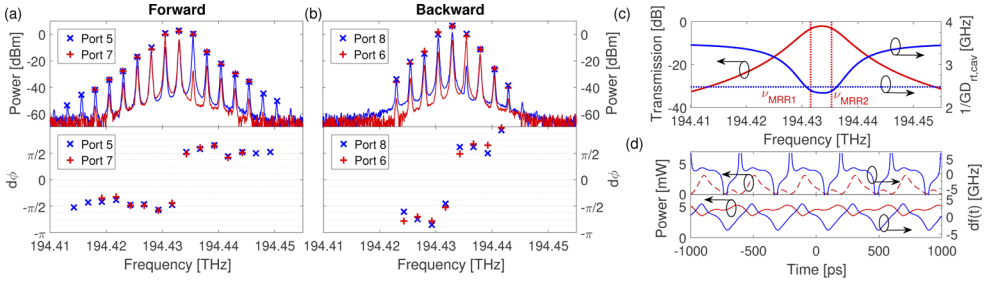

Fig. 4. (a) In the top plot is the optical spectrum of the laser at output ports 5 and 7 at a mode-locked operation point. The solid line is the measured spectrum and the crosses give the power of each line when compensated for the Vernier filter, representing the optical spectrum for the intracavity field in the forward direction. In the bottom plot is the phase difference for each line pair plotted at the frequency central to the corresponding lines for the intracavity field. (b) The same as (a) except it is the complex spectra for ports 6 and 8, and the intracavity field is for the backward direction. (c) The solid line corresponding to the left axis gives the vernier filter transmission as used for the compensation in (a) and (b) with the vertical dashed lines giving the resonance frequencies of ring 1 (ν_{MRR1}) and ring 2 (ν_{MRR2}). The solid curve corresponding to the right axis is the inverse group delay per cavity roundtrip calculated as described in Supplement 1. The horizontal dashed line gives the fundamental beating frequency found corresponding the spectra of (a) and (b). (d) Optical power (left axis) and instantaneous frequency (right axis) of the output (dashed, top) at port 5 and intracavity (solid, bottom) field propagating in the forward direction is reconstructed based on the values of spectral power per line and phase difference between comb lines measured at port 5. See Supplement 1 for uncorrected measurements of $d\phi$ and the reconstructed time traces of all other ports.

The reconstructed time trace shown in Fig. 4(d) is mostly frequency modulated which is in-line with the self-mode-locking observed in single gain section Fabry–Pérot diode lasers [22,23,26], even though the relation of $d\phi$ to frequency is quite different as here it is observed constant except for a π phase shift between the upper and lower half of the comb, whereas the single gain section Fabry–Pérot diode lasers are found to have a linear relation between $d\phi$ and frequency [24], i.e., a quadratic spectral phase relation. For future work, it would be of interest to see whether the addition of the highly dispersive Vernier filter can account for the difference in spectral phase or whether it is also due to the double gain section as the mixing leading to a phase-locked comb is different in each gain section indicated by the width of the comb, which is significantly larger leaving gain 1 [see Fig. 4(a)] compared with gain 2 [see Fig. 4(b)].

The repetition rate of the MLL is tunable in at least a 600-MHz range around 2.2 GHz by changing the overlap of the ring resonances and the location of the laser central laser cavity mode in this resonance (see Supplement 1). The tunable repetition rate is a result of the additional group delay induced by the ring resonators as can be seen in Fig. 4 (c), this delay can be adjusted by changing the overlap of the ring resonances.

To conclude, in this Letter we have demonstrated the mode-locked operation of a hybrid integrated laser comprising two gain section. Accordingly, we have shown that the intracavity field in the laser is mostly frequency modulated, which is inline with single gain section semiconductor lasers [26]. The combination of a predominantly frequency modulated field and a small comb width leads to high power per comb line.

Funding. Nederlandse Organisatie voor Wetenschappelijk Onderzoek (740.018.021); European Space Agency (40000121956/17/NL/CLP).

Acknowledgment. The authors would like to acknowledge the collaboration with partner Viasat.

Disclosures. The authors declare no conflicts of interest

Data availability. Data underlying the results presented in this paper are available in Ref. [27].

Supplemental document. See Supplement 1 for supporting content.

REFERENCES

1. N. Picqué and T. W. Hänsch, Nat. Photonics **13**, 146 (2019).
2. A. D. Ludlow, M. M. Boyd, J. Ye, E. Peik, and P. O. Schmidt, Rev. Mod. Phys. **87**, 637 (2015).
3. P. Trocha, M. Karpov, D. Ganin, M. H. P. Pfeiffer, A. Kordts, S. Wolf, J. Krockenberger, P. Marin-Palomo, C. Weimann, S. Randel, W. Freude, T. J. Kippenberg, and C. Koos, Science **359**, 887 (2018).
4. B. Corcoran, M. Tan, X. Xu, A. Boes, J. Wu, T. G. Nguyen, S. T. Chu, B. E. Little, R. Morandotti, A. Mitchell, and D. J. Moss, Nat. Commun. **11**, 2568 (2020).
5. J. Wu, X. Xu, T. G. Nguyen, S. T. Chu, B. E. Little, R. Morandotti, A. Mitchell, and D. J. Moss, IEEE J. Sel. Top. Quantum Electron. **24**, 6101020 (2018).
6. A. Pasquazi, M. Peccianti, L. Razzari, D. J. Moss, S. Coen, M. Erkintalo, Y. K. Chembo, T. Hansson, S. Wabnitz, P. Del'Haye, X. Xue, A. M. Weiner, and R. Morandotti, Phys. Rep. **729**, 1 (2018).
7. A. L. Gaeta, M. Lipson, and T. J. Kippenberg, Nat. Photonics **13**, 158 (2019).
8. K. Van Gasse, S. Uvin, V. Moskalenko, S. Latkowski, G. Roelkens, E. Bente, and B. Kuyken, IEEE Photonics Technol. Lett. **31**, 1870 (2019).
9. B. Dong, X. C. De Labriolle, S. Liu, M. Dumont, H. Huang, J. Duan, J. C. Norman, J. E. Bowers, and F. Grillot, J. Phys. Photonics **2**, 045006 (2020).
10. D. Marpaung, J. Yao, and J. Capmany, Nat. Photonics **13**, 80 (2019).
11. K.-J. Boller, A. van Rees, and Y. Fan, *et al.*, Photonics **7**, 4 (2019).
12. Y. Fan, A. van Rees, P. J. M. van der Slot, J. Mak, R. M. Oldenbeuving, M. Hoekman, D. Geskus, C. G. H. Roeloffzen, and K.-J. Boller, Opt. Express **28**, 21713 (2020).
13. W. Jin, Q.-F. Yang, L. Chang, B. Shen, H. Wang, M. A. Leal, L. Wu, M. Gao, A. Feshali, M. Paniccia, K. J. Vahala, and J. E. Bowers, Nat. Photonics **15**, 346 (2021).
14. J. Mak, A. van Rees, Y. Fan, E. J. Klein, D. Geskus, P. J. M. van der Slot, and K.-J. Boller, Opt. Express **27**, 13307 (2019).
15. H. M. J. Bastiaens, G. Neijts, A. Memon, Y. Fan, J. Mak, D. Geskus, M. Hoekman, V. Moskalenko, E. A. J. M. Bente, and K.-J. Boller, Proc. SPIE **11705**, 1170508 (2021).
16. E. Vissers, S. Poelman, C. O. de Beeck, K. Van Gasse, and B. Kuyken, Opt. Express **29**, 15013 (2021).
17. Y. Ibrahimi, S. Boust, Q. Wilmart, J.-F. Paret, A. Garreau, K. Mekhazni, C. Fortin, F. Duport, F. Van Dijk, C. Sciancalepore, S. Garcia, and J. M. Fedeli, J. Lightwave Technol. **39**, 7573 (2021).
18. A. Hermans, K. Van Gasse, J. Kjellman, C. Caër, T. Nakamura, Y. Inada, K. Hisada, T. Hirasawa, S. Cuyvers, S. Kumari, A. Marinins, R. Jansen, G. Roelkens, P. Soussan, X. Rottenberg, and B. Kuyken, APL Photonics **6**, 096102 (2021).
19. S. Cuyvers, B. Haq, C. Op de Beeck, S. Poelman, A. Hermans, Z. Wang, A. Gocalinska, E. Pelucchi, B. Corbett, G. Roelkens, K. Van Gasse, and B. Kuyken, Laser Photonics Rev. **15**, 2000485 (2021).
20. J. P. Epping, R. M. Oldenbeuving, D. Geskus, I. Visscher, R. Grootjans, C. G. Roeloffzen, and R. G. Heideman, Laser Congress 2019 (ASSL, LAC, LS&C), OSA Technical Digest (Optical Society of America, 2019), paper ATu1A.4.
21. D. A. Reid, S. G. Murdoch, and L. P. Barry, Opt. Express **18**, 19724 (2010).
22. L. Tiemeijer, P. Kuindersma, P. Thijs, and G. Rikken, IEEE J. Quantum Electron. **25**, 1385 (1989).
23. K. Sato, IEEE J. Sel. Top. Quantum Electron. **9**, 1288 (2003).
24. R. Rosales, S. G. Murdoch, R. Watts, K. Merghem, A. Martinez, F. Lelarge, A. Accard, L. P. Barry, and A. Ramdane, Opt. Express **20**, 8649 (2012).
25. C. G. H. Roeloffzen, M. Hoekman, and E. J. Klein, *et al.*, IEEE J. Sel. Top. Quantum Electron. **24**, 4400321 (2018).
26. M. Dong, S. T. Cundiff, and H. G. Winful, Phys. Rev. A **97**, 053822 (2018).
27. Y. Klaver, J. P. Epping, C. G. H. Roeloffzen, and D. A. I. Marpaung, "Intracavity time-domain characterisation of a high-power hybrid integrated laser in mode-locked operation," 4TU.ResearchData, 17 December 2021, https://dx.doi.org/10.4121/15074172.